Secondary gravitational wave signatures from 5D rotating primordial black holes in the dark dimension

Waqas Ahmed[1,*] and George K. Leontaris[2,†]

[1]*Center for Fundamental Physics, School of Artificial Intelligence, Hubei Polytechnic University, Huangshi 435003, China*

[2]*Physics Department, University of Ioannina, 45110 Ioannina, Greece*

(Received 17 May 2026; accepted 9 July 2026; published 23 July 2026)

We investigate five-dimensional rotating primordial black holes (PBHs) as dark matter candidates within the dark dimension scenario motivated by the Swampland Program. In this framework, a micron-scale extra dimension modifies Hawking evaporation, while a phenomenological memory-burden factor S^{-p} can further prolong PBH lifetimes. We compute the evaporation dynamics for rotating 5D PBHs, derive the burdened lifetime scaling, and study the fiducial $p = 2$ benchmark over $10^{10}\ \mathrm{g} \lesssim M \lesssim 10^{21}\ \mathrm{g}$. The curvature perturbations responsible for PBH formation also generate a stochastic gravitational wave background through second-order scalar-induced effects. Assuming a log-normal primordial power spectrum with $\sigma = 1$ and $f_{\mathrm{PBH}} = 1$, we calculate the present-day energy density $\Omega_{\mathrm{GW}}h^2$ across this benchmark interval. The predicted signals peak at frequencies from nHz to Hz, within the sensitivity ranges of LISA and DECIGO/BBO. Fisher forecasts illustrate the prospective sensitivity to the PBH mass, dark matter fraction, spectral width, and phenomenological exponent p. A joint test of the gravitational-wave spectrum and the evaporation history could probe extradimensional PBHs and memory-burden phenomenology.

DOI: 10.1103/8xgd-37lf

I. INTRODUCTION

A wide range of astrophysical and cosmological observations confirm the existence of dark matter in the Universe, yet its fundamental nature remains unknown. Primordial black holes (PBHs), formed from the gravitational collapse of overdense regions in the early Universe [1–4], have long been considered compelling dark matter candidates. In the standard four-dimensional framework, PBHs with masses

$$M \lesssim 5 \times 10^{14}\ \mathrm{g},$$

would have completely evaporated by the present day due to Hawking radiation [2], and thus cannot be dark matter candidates. For higher masses, stringent bounds from the extragalactic gamma-ray background [5] and constraints from the cosmic microwave background [6] severely limit their abundance, while microlensing limits [7,8] and gravitational wave merger rate studies [9] make it highly improbable for PBHs in any subrange to account for 100% of the dark matter in four dimensions.

Renewed interest in PBHs has been driven by the detection of black-hole mergers via gravitational waves [10], (some of which may have a primordial origin), together with significant theoretical progress on their formation mechanisms during inflation and cosmological phase transitions. Theoretical progress including the higher dimensional (dark dimension) scenario, the memory burden effect, or breakdown of semiclassical approximations, has indicated new mass windows for PBHs to constitute all or a significant fraction of the dark matter, by accounting for effects such as modified Hawking evaporation.

Recent developments in the Swampland Program have opened new avenues for addressing these limitations. The Swampland Distance Conjecture, originally proposed by Ooguri and Vafa [11], asserts that traversing a trans-Planckian distance in scalar field space leads to the emergence of an infinite tower of states whose masses become exponentially light. This light tower can undermine the validity and stability of the low-energy effective field theory. The conjecture, together with Bousso's covariant entropy bound [12], was shown to support a refined de Sitter conjecture and to extend naturally from AdS to de Sitter (or quasi–de Sitter) backgrounds [11,13,14]. Applying this framework to the observed smallness of

*Contact author: waqasmit@hbpu.edu.cn
†Contact author: leonta@uoi.gr

Published by the American Physical Society under the terms of the Creative Commons Attribution 4.0 International license. Further distribution of this work must maintain attribution to the author(s) and the published article's title, journal citation, and DOI. Funded by SCOAP³.

the dark energy scale Λ naturally leads to the dark dimension (DD) scenario, which predicts a single compact extra dimension of micron-scale radius R_C correlated with Λ,

$$R_C \sim \lambda \Lambda^{-1/4}, \qquad \lambda \in [10^{-1}, 10^{-4}]. \tag{1}$$

Fifth-force experiments [15,16] constrain the geometry, allowing only a single micron-size extra dimension, implying a Kaluza–Klein (KK) mass scale

$$m_{KK} \gtrsim 6.6 \text{ meV}$$

and a five-dimensional Planck scale[1]

$$M_* \sim 10^{10} \text{ GeV}.$$

The DD scenario profoundly impacts PBHs physics by suppressing Hawking radiation in higher dimensions, thus allowing lighter PBHs to survive to the present epoch [17,18].

In this work, we investigate the phenomenology of five-dimensional rotating PBHs within the framework of the dark dimension scenario. We extend previous studies of five-dimensional Schwarzschild [19,20] and rotating [21] PBHs by considering their potential role as dark matter and by analyzing in detail their Hawking evaporation, incorporating the memory burden effect. The latter is a quantum gravitational phenomenon in which the storage of information in PBHs suppresses Hawking evaporation [22].

The dark dimension plus memory-burden mechanism is not the only proposed route to long-lived light PBHs. Nearly extremal black holes can also have a strongly suppressed Hawking temperature. In particular, charged PBHs may be long lived if discharge is inhibited by a sufficiently heavy dark charged state [23], while large-N gauge theories can suppress charge loss combinatorially and drive black holes toward extremality for exponentially long times [24]. These scenarios require additional gauge-sector assumptions and are physically distinct from the neutral, five-dimensional memory-burden mechanism studied here.

In this work, we perform a systematic comparison between four- and five-dimensional dynamics and derive, in detail, the distinct mass windows for PBHs that can survive until the present epoch. Furthermore, we provide a complete derivation of the evaporation dynamics of five-dimensional rotating black holes, including the impact of the memory burden effect, and explore their connection to scalar-induced gravitational waves (SIGWs).

[1]Throughout this paper, we adopt natural units, $\hbar = c = k_B = 1$, with M_P and M_* denoting the reduced four-dimensional and fundamental five-dimensional Planck scales, respectively. The factor $\hbar$ is restored only when expressing time in seconds or years.

Our analysis also includes detailed numerical computations of the resulting stochastic gravitational wave background over a wide range of frequencies, from nHz to mHz. Finally, we explore the full parameter space in which PBHs can account for all or a fraction of the dark matter, demonstrating that even subdominant contributions can generate detectable gravitational wave signals.

The paper is organized as follows. In Sec. II, we outline the theoretical framework, including the Swampland conjectures and the dark dimension scenario. Section III reviews higher-dimensional black holes, focusing on both static and rotating solutions. In Sec. IV, we analyze the memory burden effect and its impact on primordial black hole lifetimes. In Sec. V we discuss primordial black hole formation from curvature perturbations while in Sec. VI we derive the resulting scalar-induced gravitational wave spectrum. In Sec. VII we present our numerical results, followed by observational constraints in Sec. VIII, and finally, in Sec. IX we summarize our conclusions and discuss future directions.

II. SWAMPLAND CONSTRAINTS AND DARK DIMENSION FRAMEWORK

A. The Swampland Program

The Swampland Program aims to identify the subset of low-energy effective field theories that can arise from a consistent theory of quantum gravity [25,26]. Within this framework, not every effective theory is considered viable; instead, a set of conjectured criteria is imposed to distinguish the consistent "landscape" from the inconsistent "swampland." The latter consists of theories that, despite appearing consistent at low energies, cannot be embedded into a UV-complete framework such as string theory [27–29].

A central element of this program is the *distance conjecture* [11], which states that a large excursion in scalar field space leads to the appearance of an infinite tower of light states. For a field displacement $\Delta\phi \gg 1$ (in Planck units), the mass scale of this tower behaves as

$$m \sim m_0 e^{-\alpha \Delta\phi}, \qquad \alpha = \mathcal{O}(1). \tag{2}$$

Another important constraint is the *weak gravity conjecture* [11,30], which asserts that gravity must be the weakest force in any consistent quantum gravity theory. For a $U(1)$ gauge theory with coupling g, this implies the existence of a charged state satisfying

$$\frac{m}{g M_P} \lesssim \mathcal{O}(1). \tag{3}$$

B. The AdS distance conjecture and dark energy

The distance conjecture can be extended to curved backgrounds, particularly anti–de Sitter (AdS) spacetime. The *AdS distance conjecture* [14] suggests that as the

cosmological constant $\Lambda < 0$ approaches zero, a tower of states becomes light. For the KK spectrum, this leads to

$$m_{\mathrm{KK}} \sim |\Lambda|^{a}, \qquad a = \frac{1}{4}. \tag{4}$$

Using the observed value of the cosmological constant, one obtains

$$m_{\mathrm{KK}} \sim (10^{-122} M_P^4)^{1/4} \sim 10^{-30.5} M_P \sim 10^{-3}\ \mathrm{eV}. \tag{5}$$

This corresponds to an extra dimension with characteristic size

$$R_C \sim \frac{1}{m_{\mathrm{KK}}} \sim 10\text{–}100\ \mu\mathrm{m}, \tag{6}$$

where the precise numerical value depends on the order-one coefficient relating the KK scale to $\Lambda^{1/4}$. For example, $m_{\mathrm{KK}} \gtrsim 6.6$ meV corresponds to $R_C \lesssim 30$ μm.

C. Experimental constraints

Consistency conditions from quantum field theory in curved spacetime further constrain the parameter space. In particular, the Higuchi bound [31] for massive spin-2 fields in de Sitter space restricts the exponent a to the range [21]

$$\frac{1}{4} \le a \le \frac{1}{2}. \tag{7}$$

Fifth-force experiments and precision tests of Newton's inverse-square law [32,33] further constrain the geometry of possible extra dimensions by placing strong upper bounds on deviations from $1/r$ gravity at submillimeter scales. In particular, such measurements restrict the compactification scale to the micron regime, thereby limiting the size of extra dimensions and the mass scale of the corresponding KK modes. These constraints can be interpreted as bounding the effective parameter space of the theory, effectively saturating the lower limit $a = 1/4$ in phenomenological realizations [14,34]. In the presence of compact extra dimensions, Newton's gravitational potential receives Yukawa-type corrections and can be written as

$$V(r) = -\frac{G_4 M_1 M_2}{r}(1 + \alpha e^{-r/\lambda}). \tag{8}$$

Experimental tests of the inverse-square law down to distances of order 30 μm [15,35] impose strong limits on such deviations. These results imply that any extra dimension must lie below this scale and strongly favor the existence of at most a single extra dimension in the micron range.

D. The species scale

The presence of a large number of light species lowers the effective scale at which quantum gravity becomes strongly coupled. This scale, known as the species scale [36], is particularly relevant in higher-dimensional setups.

For a single extra dimension ($n = 1$), the relation between the four-dimensional Planck scale M_P and the five-dimensional fundamental scale M_* is given by

$$M_P^2 = M_*^3 R_C, \tag{9}$$

where $R_C \sim 1/m_{\mathrm{KK}}$ is the compactification radius. This leads to

$$M_* \sim (m_{\mathrm{KK}} M_P^2)^{1/3} \sim 10^{10}\ \mathrm{GeV}. \tag{10}$$

This scale characterizes the onset of higher-dimensional gravitational effects.

E. Implications for primordial black holes

The existence of a compact extra spatial dimension at the micron scale can have significant implications for PBH physics. In such higher-dimensional frameworks, the process of Hawking radiation is modified due to the altered gravitational phase space and the emergence of additional KK modes, which leads to a deviation from the standard four-dimensional evaporation rate [37–39].

The parametric origin of the different mass dependence is transparent. For a neutral Schwarzschild-Tangherlini black hole in $D = 4 + n$ dimensions, $A_{D-2} \propto r_H^{D-2}$ and $T_H \propto r_H^{-1}$. A thermal channel propagating in the full D-dimensional phase space therefore carries power

$$P_D \sim A_{D-2} T_H^D \sim r_H^{-2}. \tag{11}$$

Since $r_H \propto M^{1/(n+1)}$, this gives $-\dot{M} \propto M^{-2/(n+1)}$ and $\tau_D \propto M^{(n+3)/(n+1)}$. Thus $\tau_4 \propto M^3$, whereas $\tau_5 \propto M^2$. Greybody factors and the numbers of brane and bulk degrees of freedom determine the dimensionless coefficient but do not alter these powers. Additional KK channels by themselves do not guarantee slower evaporation; the longer lifetime at fixed mass in the parameter range used below follows from the five-dimensional radius-temperature relation and the resulting normalization of the emission rate.

The phenomenological structure of PBHs also depends crucially on whether they are confined to a four-dimensional brane or allowed to probe the higher-dimensional bulk. In brane-localized scenarios, the emission spectrum is effectively restricted to Standard Model degrees of freedom on the brane, leading to comparatively faster evaporation. In contrast, bulk-propagating configurations allow additional gravitational channels, which modify the temperature-mass relation and can slow down the evaporation process [38–40]. These differences naturally translate into

distinct mass windows for PBHs that can survive until the present epoch.

For brane-localized black holes, the viable mass range is typically

$$10^{15} \lesssim \frac{M_{\rm BH}}{\rm g} \lesssim 10^{21}, \tag{12}$$

whereas in higher-dimensional or bulk-dominated scenarios the modified evaporation dynamics can relax the lower bound to

$$10^{10} \lesssim \frac{M_{\rm BH}}{\rm g} \lesssim 10^{21}. \tag{13}$$

These differences arise from the modified Hawking temperature and enhanced emission channels in higher-dimensional gravity, which directly affect the evaporation timescale [39,40].

This framework is particularly relevant in light of recent developments connecting extradimensional physics with cosmological observations and quantum gravity constraints, where compact dimensions at submillimeter scales naturally emerge in phenomenological models addressing hierarchy and dark sector physics [19,41,42].

III. HIGHER-DIMENSIONAL BLACK HOLES: STATIC AND ROTATING SOLUTIONS

The spacetime geometry of a higher-dimensional black hole critically depends on the distance scale relative to the compactification radius R_C. At distances much smaller than R_C ($r \ll R_C$), the gravitational field propagates in all $4+n$ dimensions, and the black hole geometry is approximately that of a higher-dimensional Schwarzschild-Tangherlini solution [43],

$$ds^2 = -h(r)dt^2 + \frac{dr^2}{h(r)} + r^2 d\Omega_{n+2}^2, \tag{14}$$

where

$$h(r) = 1 - \left(\frac{r_H}{r}\right)^{n+1}, \tag{15}$$

and r_H is the horizon radius, with $d\Omega_{n+2}^2$ representing the metric on a unit $(n+2)$-sphere. For one extra dimension ($n=1$), the horizon radius is [44],

$$r_S = \left(\frac{8}{3\pi}\frac{M_{\rm BH}}{M_*}\right)^{\frac{1}{2}} \frac{1}{M_*}. \tag{16}$$

The ratio r_H/R_C determines whether a neutral black hole is effectively five-dimensional ($r_H \ll R_C$) or appears four-dimensional to brane-localized observers ($r_H \gg R_C$). Figure 1 displays this ratio as a function of the black hole mass M, using the 5D Planck scale $M_* = 10^{10}$ GeV and a compactification radius $R_C = 1$ μm characteristic of the dark dimension scenario [14]. The shaded green band indicates the mass window $10^{10}\ \text{g} \lesssim M \lesssim 10^{21}\ \text{g}$ that is phenomenologically relevant for primordial black hole dark matter candidates (see Sec. III D). The crossing point $M \approx 1.69 \times 10^{26}$ g, where $r_H = R_C$, marks the boundary between the two geometric regimes.

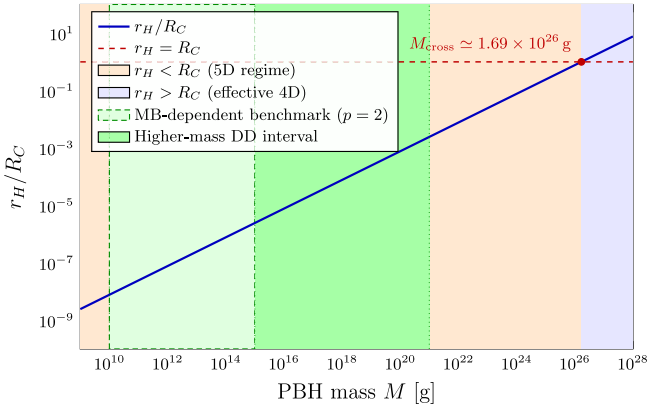


FIG. 1. Ratio of the five-dimensional Schwarzschild radius r_H to the compactification radius R_C as a function of the black hole mass M (in grams). The 5D Planck scale is fixed to $M_* = 10^{10}$ GeV and $R_C = 1$ μm. The red dashed line marks $r_H = R_C$. For $r_H \ll R_C$ (orange shaded region, left of the dashed line) the black hole is much smaller than the extra dimension; it does not "see" the compactness and behaves as a genuine five-dimensional object (Tangherlini black hole). For $r_H \gg R_C$ (light blue shaded region, right of the dashed line) the horizon wraps around the extra dimension, which is effectively averaged out, and the black hole follows the 4D Einstein equations (4D effective regime). The green shaded band highlights the dark dimension benchmark interval $10^{10}\ \text{g} \lesssim M \lesssim 10^{21}$ g. It is not an unconditional exclusion plot. The light green dashed region, $10^{10}\ \text{g} \lesssim M \lesssim 10^{15}$ g, denotes the memory-burden-dependent benchmark evaluated with $p = 2$, whereas the darker green region, $10^{15}\ \text{g} \lesssim M \lesssim 10^{21}$ g, does not rely on that assumption in the analysis of this work. The crossing point $M \approx 1.69 \times 10^{26}$ g marks the transition between the two regimes.

This geometric criterion $r_H \ll R_C$ applies to neutral primordial black holes. If a PBH carries a conserved Standard Model charge, its gauge flux is brane localized, and the neutral Tangherlini solution is not sufficient; a brane localized PBH solution is required. Such objects would exhibit 4D electromagnetic behavior on the brane. However, for the mass ranges of interest, any SM charge is rapidly neutralized by accretion, and our calculation applies to the neutral case. Hidden-sector charge capable of preventing discharge belongs to the extremal scenarios discussed in the Introduction.

The Hawking temperature in $4+n$ dimensions is

$$T_{\rm BH} = \frac{n+1}{4\pi r_S}, \tag{17}$$

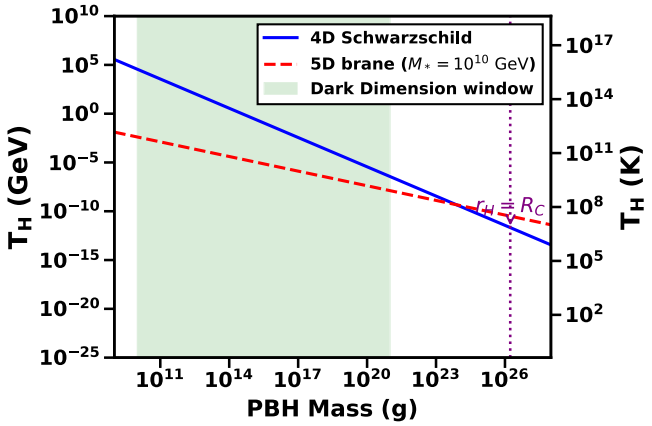


FIG. 2. Hawking temperature T_H as a function of the black hole mass M. The blue solid curve shows the standard 4D result $T_H \propto 1/M$, while the red dashed curve corresponds to a 5D brane-localized black hole with $M_* = 10^{10}$ GeV. The green shaded band marks the dark dimension window $10^{10}\ \mathrm{g} \lesssim M \lesssim 10^{21}$ g. The vertical purple line indicates the geometric transition mass $M_{\mathrm{cross}} \approx 1.69 \times 10^{26}$ g where $r_H = R_C$. For masses much smaller than this, the black hole is in the 5D regime; for masses much larger, the extra dimension is averaged out and the black hole approaches 4D behavior. The temperature crossing ($T_{4D} = T_{5D}$) occurs at a much lower mass, $M \sim 10^{21}$ g, near the upper edge of the dark dimension window. For a reference mass of 10^{15} g, the 5D temperature is orders of magnitude lower than its 4D counterpart, illustrating the suppression of Hawking radiation in the 5D scenario. The right vertical axis shows the temperature in Kelvin for convenience.

which for $n = 1$ reduces to

$$T_{\mathrm{BH}} = \frac{1}{2\pi r_S}. \tag{18}$$

Figure 2 compares the 4D and 5D temperatures. The 5D temperature is suppressed relative to the 4D case for masses below $\sim 10^{21}$ g (the crossing point where $T_{4D} = T_{5D}$), while for higher masses the ordering is reversed. The geometric transition at $r_H = R_C$ ($M \approx 1.69 \times 10^{26}$ g) is indicated by the purple vertical line; note that this is far above the temperature crossing. The geometric transition lies far above the dark dimension window $10^{10}\ \mathrm{g} \lesssim M \lesssim 10^{21}$ g, while the temperature crossing lies near its upper edge. Across the benchmark window the 5D temperature is lower than the 4D temperature. This suppression is the key feature that prolongs the lifetime of 5D primordial black holes and allows them to survive as dark matter candidates, especially when combined with the memory burden effect.

More generally, combining the horizon-radius and temperature relations gives

$$r_H \propto M^{1/(n+1)}, \quad T_H \propto M^{-1/(n+1)}, \quad M \propto T_H^{-(n+1)}. \tag{19}$$

These relations explain the logarithmic slopes in Fig. 2: $T_H \propto M^{-1}$ in four dimensions and $T_H \propto M^{-1/2}$ in five dimensions.

The entropy for n extra dimensions follows from the Smarr relation,

$$S = \frac{n+1}{n+2}\frac{M_{\mathrm{BH}}}{T_{\mathrm{BH}}}, \tag{20}$$

and for $n = 1$,

$$S = \frac{2}{3}\frac{M_{\mathrm{BH}}}{T_{\mathrm{BH}}} = \frac{4\pi}{3} M_{\mathrm{BH}} r_S. \tag{21}$$

For rotating black holes in five dimensions, the Myers-Perry solution [44] provides the appropriate metric. In Boyer-Lindquist coordinates, assuming a single nonzero angular parameter aligned with the brane, the metric reduces to,

$$ds^2 = \left(1 - \frac{\mu}{\Sigma(r,\theta) r^{n-1}}\right) dt^2 + \frac{2a\mu \sin^2\theta}{\Sigma(r,\theta) r^{n-1}} dt d\phi - \frac{\Sigma(r,\theta)}{\Delta(r)} dr^2 - \Sigma(r,\theta) d\theta^2 - \left(r^2 + a^2 + \frac{a^2 \mu \sin^2\theta}{\Sigma(r,\theta) r^{n-1}}\right) \sin^2\theta d\phi^2, \tag{22}$$

where

$$\Delta(r) = r^2 + a^2 - \frac{\mu}{r^{n-1}}, \quad \Sigma(r,\theta) = r^2 + a^2 \cos^2\theta. \tag{23}$$

Here, μ is related to the mass, and $a = J/M$ is the rotation parameter. The event horizon satisfies

$$r_H^{n+1}(1 + a_*^2) = \mu, \qquad a_* \equiv \frac{a}{r_H}, \tag{24}$$

so that

$$r_H = r_S (1 + a_*^2)^{1/(n+1)}, \qquad r_S = \mu^{1/(n+1)}. \tag{25}$$

The physical mass and angular momentum are

$$M_{\mathrm{BH}} = \frac{(n+2) A_{n+2}}{16\pi G_{4+n}} \mu, \qquad J = \frac{2}{n+2} M_{\mathrm{BH}} a, \tag{26}$$

with $A_{n+2} = \frac{2\pi^{(n+3)/2}}{\Gamma\left(\frac{n+3}{2}\right)}$ being the area of a unit $(n+2)$-sphere. For $n = 1$,

$$M_{\mathrm{BH}} = \frac{3}{16\pi G_5} A_3 \mu, \quad J = \frac{3}{2} M_{\mathrm{BH}} a, \quad A_3 = 2\pi^2. \tag{27}$$

The Hawking temperature for a rotating black hole is

$$T_{\mathrm{BH}} = \frac{1}{4\pi r_H} \frac{n + 1 + (n-1) a_*^2}{1 + a_*^2}, \tag{28}$$

and for $n = 1$,

$$T_{\rm BH} = \frac{1}{2\pi r_H(1+a_*^2)}. \tag{29}$$

The angular velocity at the horizon is

$$\Omega_H = \frac{a_*}{r_H(1+a_*^2)}. \tag{30}$$

The emission spectrum for a mode with quantum numbers (s, ℓ, m) is

$$\frac{d^3E_{s\ell m}}{d\omega dt d\theta} = \frac{1}{2\pi}\frac{s\Gamma_{\ell m}(\omega)\omega}{\exp\left[(\omega - m\Omega)/T_H\right] - (-1)^{2s}} \times \int_0^{2\pi} |sS_{\ell m}(\theta, a\omega)|^2 d\phi, \tag{31}$$

where the greybody factors $\Gamma^s_{\ell m}(\omega)$ encode the probability of escape from the black hole potential, and the total mass loss rate is

$$-\frac{dM}{dt} = \frac{1}{2\pi}\sum_{s,\ell,m} g_s \int_0^\infty \frac{s\Gamma_{\ell m}(\omega)\omega}{\exp\left[(\omega - m\Omega)/T_H\right] - (-1)^{2s}} d\omega, \tag{32}$$

with degrees of freedom $g_0 = 4$ (scalars), $g_{1/2} = 90$ (fermions), and $g_1 = 24$ (vectors) at temperature T_H. In the low-frequency regime $\omega r_H \ll 1$, greybody factors can be computed analytically [39].

Finally, the dimensionless parameter

$$\tilde{Q} = \frac{\omega - m\Omega}{2\pi T_H} = (1+a_*^2)\tilde{\omega} - ma_*, \tag{33}$$

controls the frequency dependence of the greybody factors. This unified framework sets the stage for discussing primordial black hole formation, evaporation, and evolution in higher-dimensional spacetimes.

A. Evaporation dynamics of five-dimensional rotating primordial black holes

Primordial black holes with rotation present a richer evaporation dynamics compared to nonrotating counterparts. The evolution of both mass M and angular momentum J is coupled, with the time evolution governed by [45,46],

$$\frac{dM}{dt} = -\frac{C_M(a_*)}{r_H^2}, \qquad \frac{dJ}{dt} = -\frac{C_J(a_*)}{r_H}, \tag{34}$$

where $C_M(a_*)$ and $C_J(a_*)$ are dimensionless coefficients derived from integrating greybody factors over all emission modes. The factors of r_H have been displayed explicitly in natural units. Table I lists representative values for different dimensionless spin parameters a_*.

TABLE I. Coefficients C_M and C_J for different rotation parameters a_* and their ratio $\eta = C_M/C_J$.

a_*	C_M	C_J	η
0.5	0.07	0.11	0.64
1.0	0.11	0.22	0.50
1.5	0.05	0.14	0.33

Eliminating time between these equations yields a direct relation between mass and angular momentum,

$$\frac{dJ}{dM} = \frac{1}{\eta} r_H. \tag{35}$$

For a five-dimensional rotating black hole ($n = 1$) with $G_5 = 1/(8\pi M_*^3)$, the horizon radius satisfies

$$r_H^2 = \kappa\left(1 - \lambda\frac{J^2}{\kappa}\right), \tag{36}$$

where

$$\kappa = \frac{8G_5M^3}{\pi}, \qquad \lambda = \frac{9}{4}M^2. \tag{37}$$

The extremal angular momentum is therefore $J^2_{\rm max} = \kappa/\lambda$, and a normalized spin parameter can be defined as $L = J/J_{\rm max}$ with $L \le 1$. In terms of L, the horizon radius becomes

$$r_H = \pi M_* \sqrt{\frac{3M}{M_*}(1 - L^2)}. \tag{38}$$

Substituting into the mass-angular momentum relation, the evolution equation for L reads

$$\frac{dL}{1 - L^2 - \eta L} = \frac{3}{2}\eta\frac{dM}{M}. \tag{39}$$

Integrating gives an implicit relation between M and L,

$$f(L) - f(L_0) = \frac{2}{3}\left(\eta + \frac{1}{\eta}\right)\ln\frac{M}{M_0}, \qquad f(L) = \sin^{-1}L - \eta\ln(1 - L^2 - \eta L), \tag{40}$$

which can be inverted to express M as a function of L,

$$M(L) = M_0\left(\frac{1 - L^2 - \eta L}{1 - L_0^2 - \eta L_0}\right)^{\eta\zeta}\exp\left[\zeta(\sin^{-1}L - \sin^{-1}L_0)\right], \qquad \zeta = \frac{3}{2}\eta. \tag{41}$$

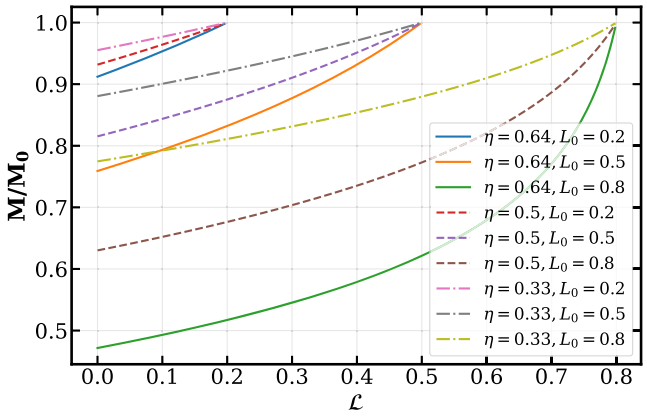


FIG. 3. Evolution of the mass fraction M/M_0 as a function of the normalized angular momentum $\mathcal{L} = J/J_{\max}$ for five-dimensional rotating black holes. Solid, dashed, and dash-dotted lines correspond to $\eta = 0.64$, 0.50, 0.33 (i.e., rotation parameters $a_* = 0.5$, 1.0, 1.5), while colours indicate different initial spins $\mathcal{L}_0$ ranging from 0.2 to 0.95. Higher initial spin results in a longer spin-down phase and a larger mass loss (typically 40%–60% of the initial mass is radiated away before the black hole becomes nonrotating).

Figure 3 illustrates the coupled evolution of mass and angular momentum during the spin-down phase. Curves are obtained by numerically inverting the implicit relation for different η and initial spins $\mathcal{L}_0$. Higher initial spin results in a longer spin-down phase and larger mass loss (typically 40%–60% of the initial mass is radiated away). The spin-down timescale is $\tau_{\rm sp} \approx 5.2 \times 10^{-15}(M_i\mathrm{g})^2$ years; for $M_i = 5 \times 10^{11}$ g, $\tau_{\rm sp} \approx 3.3 \times 10^9$ years.

Once the black hole reaches $L = 0$, it enters the nonrotating Schwarzschild phase. The remaining mass $M_f \sim 0.4$–$0.6M_i$ has a lifetime $\tau_{\rm Sch} \approx 9 \times 10^{-15}(M_f\mathrm{g})^2$ years, giving $\tau_{\rm Sch} \approx 2 \times 10^8$ years for $M_f = 1.5 \times 10^{11}$ g. The total lifetime $\tau_{\rm total} = \tau_{\rm sp} + \tau_{\rm Sch} \approx 3.5 \times 10^9$ years is comparable to the age of the Universe, demonstrating that 5D rotating PBHs with initial masses as low as 10^{11} g can survive to the present, unlike in 4D where the threshold is $M \gtrsim 5 \times 10^{14}$ g. These results highlight the crucial role of rotation in PBH evaporation dynamics, extending lifetimes and potentially affecting their contribution to the dark matter content of the Universe.

B. Memory burden and the evaporation of primordial black holes

The standard semiclassical treatment of black hole evaporation, as derived by Hawking, predicts that black holes emit thermal radiation [37], seemingly erasing all information about the matter that formed them. This apparent loss of information leads to a direct conflict with the principles of quantum mechanics, a problem known as the black hole information paradox [47]. Addressing this paradox is crucial for understanding the ultimate fate of PBHs and their potential role as dark matter candidates [17,48].

A compelling resolution has been proposed through the concept of the *memory burden effect* [49,50]. In this framework, as a black hole loses mass through Hawking radiation, information about its initial state is not lost; instead, it becomes encoded in the remaining degrees of freedom of the black hole. This accumulated information effectively acts as a feedback mechanism, gradually suppressing the evaporation rate and stabilizing the black hole against complete dissipation [51].

Mathematically, this behavior can be captured by a Hamiltonian describing a master mode and a set of memory modes [50],

$$\hat{H} = \epsilon_0 \hat{n}_0 + \hat{E}_K \sum_{k=1}^{N_m} \hat{n}_k, \tag{42}$$

where the energy gap of the memory modes depends on the occupation of the master mode [51],

$$\hat{E}_K = \left(1 - \frac{\hat{n}_0}{N_c}\right)^p \epsilon_K. \tag{43}$$

Here, N_c represents the critical occupation number, related to the black hole's entropy S, p is a parameter controlling the strength of the memory burden effect, and ϵ_0 and ϵ_K are characteristic energy scales. At early stages of evaporation, when $\hat{n}_0 \ll N_c$, memory modes carry the full energy cost $\hat{E}_K \approx \epsilon_K$. As the black hole approaches the critical occupation number, $\hat{n}_0 \to N_c$, the energy cost vanishes, $\hat{E}_K \to 0$, creating an effective energy barrier that slows further evaporation.

At present, p is not fixed by a complete microscopic theory of an evaporating black hole. In the prototype Hamiltonian it specifies how the memory-mode gap closes as the master mode approaches criticality. A linear closing gives $p = 1$, while $p = 2$ can arise when the leading variation is quadratic. These are benchmark choices rather than equally weighted predictions. Nothing in the effective description forbids $p = 3$; it gives a later onset and a stronger entropy suppression. We focus on $p = 1$ and $p = 2$ to compare the minimal linear and quadratic cases, while $p \geq 3$ belongs to the same phenomenological family and would generally make the burdened PBH even longer lived [22,52].

Mapping these quantities onto black hole parameters yields

$$\epsilon_0 = r_S^{-1}, \quad N_c = S, \quad N_m = \frac{S}{2}, \quad \epsilon_K = \sqrt{S} r_S^{-1}, \tag{44}$$

with r_S the Schwarzschild radius and S the Bekenstein-Hawking entropy [53]. The onset of the memory burden phase occurs after a critical fraction of the black hole mass has been lost,

$$q \equiv \frac{\Delta M_{\rm crit}}{M_0} \sim (pS)^{-1/p}, \tag{45}$$

illustrating that the timing of this effect strongly depends on the parameter p. For $p = 1$, $q \sim S^{-1}$, while $p = 2$ and $p = 3$ give $q \sim S^{-1/2}$ and $q \sim S^{-1/3}$, respectively, up to order-one factors. Thus increasing p delays the onset, but an order-one mass loss is reached only for parametrically large p, of order $\ln S$; it is not implied for every $p > 1$.

We implement the burdened phase through the standard phenomenological ansatz that the Hawking rate is multiplied by S^{-p} [22],

$$\left.\frac{dM}{dt}\right|_{\rm MB} = S^{-p}\left.\frac{dM}{dt}\right|_{\rm H} = -\frac{C_M}{r_H^2 S^p}. \tag{46}$$

This equation is an effective post-onset parametrization, not a derivation of p from first principles. The factor r_H^{-2} is the Hawking power derived in Eq. (11), and S^{-p} is the assumed memory-burden suppression; no additional factor of M is present. For a five-dimensional Schwarzschild black hole, define

$$x \equiv \frac{M}{M_*}, \qquad r_H = \frac{a_5}{M_*}x^{1/2}, \qquad S = s_5 x^{3/2},$$
$$a_5 = \sqrt{\frac{8}{3\pi}}, \qquad s_5 = \frac{4\pi}{3}a_5. \tag{47}$$

Equation (46) then becomes

$$\frac{dM}{dt} = -\frac{C_M M_*^2}{a_5^2 s_5^p} x^{-1-3p/2}. \tag{48}$$

Integrating from M_i to M_f gives

$$\tau^{(p)}(M_i \to M_f) = \frac{2a_5^2 s_5^p}{C_M(3p+4)M_*} \times \left[\left(\frac{M_i}{M_*}\right)^{2+3p/2} - \left(\frac{M_f}{M_*}\right)^{2+3p/2}\right]. \tag{49}$$

For $M_f \ll M_i$, this yields $\tau^{(p)} \propto M_i^{2+3p/2}$: M^2, $M^{7/2}$, and M^5 for $p = 0, 1, 2$, respectively. For the dark dimension scenario, the five-dimensional Planck scale is $M_* = 10^{10}$ GeV and the coefficient is $C_M \approx 0.04$. Converting to years (using $\hbar$ and the number of seconds per year), we obtain the following numerical approximations:

$$\tau^{(p=0)}(M) = 6.96 \times 10^{-14}\left(\frac{M}{\rm g}\right)^2 \text{ years}, \tag{50}$$

$$\tau^{(p=1)}(M) = 6.45 \times 10^{7}\left(\frac{M}{\rm g}\right)^{7/2} \text{ years}, \tag{51}$$

TABLE II. PBH lifetime comparison under standard Hawking evaporation and with the phenomenological memory-burden (MB) factor S^{-p} in five dimensions. These entries compare total lifetimes only; they do not by themselves constitute big bang nucleosynthesis (BBN) or CMB exclusion limits.

Mass (g)	4D Hawking (yr)	5D no MB (yr)	5D MB $p = 1$ (yr)	5D MB $p = 2$ (yr)
10^{10}	1.0×10^{-5}	7.0×10^{6}	6.5×10^{42}	7.3×10^{78}
10^{12}	1.0×10^{1}	7.0×10^{10}	6.5×10^{49}	7.3×10^{88}
10^{15}	1.0×10^{10}	7.0×10^{16}	2.0×10^{60}	7.3×10^{103}
10^{18}	1.0×10^{19}	7.0×10^{22}	6.5×10^{70}	7.3×10^{118}

$$\tau^{(p=2)}(M) = 7.32 \times 10^{28}\left(\frac{M}{\rm g}\right)^5 \text{ years}. \tag{52}$$

These formulas demonstrate that even relatively light black holes can remain stable over cosmological timescales. For example, in the postonset ansatz of Eq. (46), a PBH of mass 10^{10} g has a lifetime longer than the age of the Universe for both $p = 1$ and $p = 2$, with the suppression much stronger for $p = 2$. Lifetime alone, however, is not sufficient to establish cosmological viability; the time-dependent luminosity and the onset of the burdened phase must also be included. To illustrate the lifetime scaling, Table II compares PBHs of different masses under several evaporation scenarios. The detailed analysis of PBH formation is presented in the next Section.

C. Energy injection constraints in the burdened phase

A PBH can survive to the present day (a total lifetime $\tau_{\rm total} > t_U$) without necessarily being cosmologically viable. The crucial quantity is not the total lifetime, but the rate of energy injection $\dot{M}(t)$ in various cosmological epochs.

Even if a PBH survives until today, its Hawking emission during BBN ($t \sim 1 - 10^3$ s), or around recombination ($t \sim 10^{13}$ s) may still produce observable cosmological signatures, such as,

(i) Alterations of the primordial light-element abundances (D, ^{3}He, ^{4}He, ^{7}Li) through photodissociation and hadronic cascades;

(ii) μ-type and y-type spectral distortions of the CMB.

These constraints are well-established in the PBH literature [17,54–57] and are independent of the specific PBH formation mechanism.

For $p = 1$, the estimate in Eq. (45) gives $q \sim S^{-1} \ll 1$, so the burdened phase begins after a very small fractional mass loss. The postonset luminosity is then reduced by S^{-1} and the lifetime scales as $M^{7/2}$. For $p = 2$, the onset occurs after $q \sim (2S)^{-1/2}$ and the post-onset rate is suppressed by S^{-2}, yielding $\tau \propto M^5$. The $p = 2$ benchmark is therefore more strongly stabilized, but it does not have a later onset than every $p > 1$ in the sense of an order-one mass loss; such a late onset requires parametrically larger p.

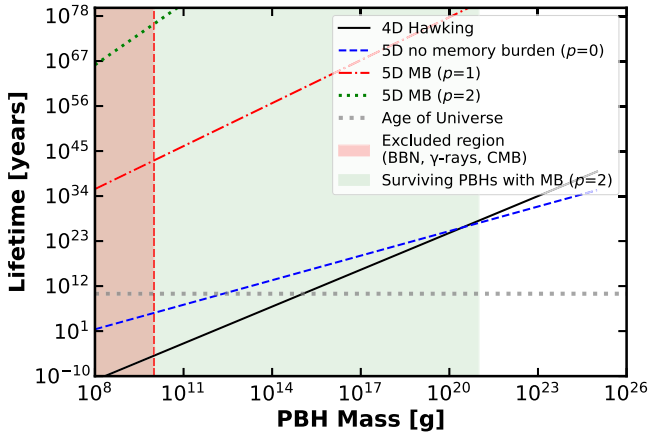


FIG. 4. PBH lifetime as a function of initial mass for different evaporation scenarios, computed using Eq. (49). The curves illustrate the distinct mass scalings for $p = 0, 1, 2$. The horizontal line marks the age of the Universe. The red/orange bands summarize mass ranges constrained under standard evaporation assumptions; they must not be read as direct exclusions of the $p = 1$ or $p = 2$ curves without recomputing the time-dependent burdened luminosity and energy deposition. The green interval identifies the fiducial $p = 2$ benchmark used in the subsequent gravitational-wave analysis.

Standard BBN, gamma-ray, and CMB limits are derived for a specified time-dependent Hawking luminosity and cannot be applied to a burdened PBH by comparing its total lifetime with an exclusion band. They must be recomputed using $f_{\rm PBH}|\dot{M}(t)|$ and the emitted spectrum after the onset. We therefore use $p = 2$ as the fiducial, strongly suppressed benchmark that defines the lower green interval in Figs. 1 and 4, but we no longer claim that $p = 1$ or $p = 3$ is excluded solely by the lifetime plot. A dedicated energy-deposition analysis for each p is beyond the scope of the present work.

D. Primordial black hole formation and mass distribution

PBHs can form in the early Universe if sufficiently large curvature perturbations produced during inflation reenter the Hubble horizon during the radiation-dominated epoch and undergo gravitational collapse [1,2,58]. When a perturbation mode reenters the horizon, the corresponding overdense region may collapse into a black hole if the density contrast exceeds a critical threshold. The density contrast is defined as

$$\delta = \frac{\delta\rho}{\rho}, \tag{53}$$

whilst numerical simulations indicate that gravitational collapse occurs [59,60] when

$$\delta > \delta_c \simeq 0.45. \tag{54}$$

The mass of the PBH at formation is expected to be comparable to the mass contained within the Hubble horizon at the time of reentry. This can be expressed as

$$M_{\rm PBH} \simeq \gamma M_H = \gamma \frac{4\pi}{3}\rho H^{-3}\Big|_{\text{re-entry}}, \tag{55}$$

where $\gamma \simeq 0.2$ [17,61] characterizes the efficiency of the collapse process.

During the radiation-dominated epoch, the horizon mass is related to the Hubble parameter through [62]

$$M_H = \frac{1}{2GH}; \qquad k = aH. \tag{56}$$

In the above, k denotes the comoving wave number of the perturbation mode. By combining entropy conservation with the temperature evolution of the Universe, we obtain a relation between the PBH mass and the corresponding comoving scale,

$$k \simeq 7 \times 10^6 \left(\frac{10^{15}\ \text{g}}{M_{\rm PBH}}\right)^{\frac{1}{2}} \left(\frac{g_*}{106.75}\right)^{\frac{1}{4}} \left(\frac{3.36}{g_{*0}}\right)^{\frac{1}{3}} \text{Mpc}^{-1}, \tag{57}$$

where g_* and g_{*0} represent the effective relativistic degrees of freedom at the time of PBH formation and at present, respectively.

The creation of PBHs is highly sensitive to the amplitude of primordial curvature perturbations, which are characterized by the curvature power spectrum $\mathcal{P}_s(k)$. In many PBH formation scenarios, the spectrum exhibits a localized enhancement at small scales, often generated by features in the inflationary potential. This enhancement is commonly modeled by a log-normal form [63,64],

$$\mathcal{P}_s(k) = \frac{A_{\mathcal{R}}}{\sqrt{2\pi}\sigma} \exp\left[-\frac{\ln^2(k/k_*)}{2\sigma^2}\right], \tag{58}$$

where $A_{\mathcal{R}}$ is the integrated amplitude (related to the variance) at the peak scale k_*, and σ determines the logarithmic width of the peak. It should be noted that the log-normal shape provides a flexible phenomenological description, where in the limit $\sigma \to 0$ approaches a monochromatic spectrum, whilst nonzero and larger σ values represent a broad enhancement.

The variance of curvature perturbations is obtained by integrating the power spectrum over logarithmic wave number intervals,

$$\langle \mathcal{R}^2 \rangle = \int_0^\infty \mathcal{P}_{\mathcal{R}}(k) d\ln k. \tag{59}$$

For sufficiently narrow enhancement in the spectrum, the dominant contribution originates from scales in the vicinity

of k_*. In this case, the integral is approximately equal to the peak amplitude times the effective width. However, with the normalization chosen in Eq. (58), the integral yields exactly $A_{\mathcal{R}}$ irrespective of σ because the distribution is normalized to unity,

$$\int_0^\infty \frac{1}{\sqrt{2\pi}\sigma}\exp\left[-\frac{\ln^2(k/k_*)}{2\sigma^2}\right]d\ln k = 1,$$

so that $\langle\mathcal{R}^2\rangle = A_{\mathcal{R}}$. Observe that for this conventional parameterization, the variance is given directly by $A_{\mathcal{R}}$, independent of the width σ. This makes $A_{\mathcal{R}}$ a convenient measure of the overall power in the peak.

The abundance of PBHs produced from these fluctuations can be estimated using the Press-Schechter formalism [65]. In this framework, the fraction of horizon patches collapsing into PBHs at a mass scale M is given by

$$\beta(M) = \int_{\delta_c}^\infty P(\delta_R)d\delta_R = \frac{1}{2}\mathrm{erfc}\left(\frac{\delta_c}{\sqrt{2}\sigma(M)}\right), \tag{60}$$

where $\sigma(M)$ is the variance of density fluctuations on the corresponding scale. For a sharply peaked power spectrum one can approximate

$$\sigma^2(M) \simeq \mathcal{P}_{\mathcal{R}}(k). \tag{61}$$

Non-Gaussian features in primordial fluctuations can also influence the probability of PBH formation. In the presence of non-Gaussianity of local type, characterized by the parameter f_{NL}, the probability distribution of curvature perturbations deviates from the standard Gaussian form. Positive non-Gaussianity enhances the probability of large fluctuations and therefore increases the PBH formation rate, while negative non-Gaussianity has the opposite effect [66–68].

The resulting PBH population is described by a mass function $\psi(M)$, defined as

$$\psi(M) = \frac{M}{\rho_{\mathrm{CDM}}}\frac{dn}{dM}, \tag{62}$$

where dn/dM is the density per unit mass interval and ρ_{CDM} is the density of cold dark matter. The total fraction of dark matter in PBHs is then

$$f_{\mathrm{PBH}} = \int_0^\infty \psi(M)dM = \frac{\rho_{\mathrm{PBH}}}{\rho_{\mathrm{CDM}}}. \tag{63}$$

For PBHs originating from a peaked primordial spectrum, the mass distribution is often well approximated by a log-normal function [65,69]

$$\psi(M) = \frac{f_{\mathrm{PBH}}}{\sqrt{2\pi}\sigma_m M}\exp\left[-\frac{\ln^2(M/M_*)}{2\sigma_m^2}\right], \tag{64}$$

where M_* indicates the peak mass and σ_m represents the width of the distribution in logarithmic mass space. In the next Section, we discuss the associated gravitational-wave signatures in detail.

IV. FROM FIVE-DIMENSIONAL GRAVITY TO SCALAR-INDUCED GRAVITATIONAL WAVES

In theories with a single compact extra dimension, the five-dimensional Einstein equations reduce to an effective four-dimensional description for tensor perturbations on the brane, provided the physical wavelengths of interest are much larger than the compactification radius $R_C \sim \mu\mathrm{m}$ (i.e., the corresponding momenta are well below the KK mass scale $m_{\mathrm{KK}} = 1/R_C$) [70,71]. The extra dimension is compactified at a scale $R_C \sim \mu\mathrm{m}$ [14], which is much smaller than any cosmological horizon relevant for PBH formation or gravitational-wave production [72,73]. Under this condition, the zero mode of the five-dimensional graviton corresponds to the usual massless four-dimensional graviton, while the massive KK excitations are too heavy to be excited and therefore do not contribute significantly to the dynamics [74,75]. Consequently, the propagation of tensor perturbations at cosmological scales is effectively four dimensional, allowing the standard SIGW formulas to be applied within the dark dimension scenario [76–78].

To explore the dynamics of tensor perturbations in a scenario with an extra dimension, we begin with the five-dimensional Einstein–Hilbert action [75,79]

$$S_5 = \frac{1}{2\kappa_5^2}\int d^4x dy\sqrt{-g_5}R_5, \tag{65}$$

where $\kappa_5^2 = 8\pi G_5 = M_*^{-3}$, and $M_* \sim 10^{10}$ GeV represents the fundamental Planck scale in five dimensions. Here, y stands for the coordinate along the extra dimension, which is compactified on a circle of radius R_C with periodic boundary conditions.

We consider a 5D spacetime metric of the form

$$ds_5^2 = g_{\mu\nu}(x,y)dx^\mu dx^\nu + dy^2, \tag{66}$$

where, in general, $g_{\mu\nu}(x,y)$ may depend on the extra coordinate y, while cross terms are not included and thus the compact extra dimension is taken to be orthogonal to the 4D spacetime [74].

Expanding around a four-dimensional Friedmann-Lemaître-Robertson-Walker (FLRW) background, the metric can be expressed as

$$g_{\mu\nu}(x,y) = a^2(\tau)[\eta_{\mu\nu} + h_{\mu\nu}(x,y)], \tag{67}$$

where $a(\tau)$ is the scale factor as a function of conformal time τ, and $h_{\mu\nu}$ represents small perturbations of the metric [80,81].

Linearizing the five-dimensional Einstein equations and working in the transverse-traceless gauge, the evolution of the tensor perturbations is governed by [74]

$$(\Box_4 + \partial_y^2)h_{\mu\nu} = -16\pi G_5 T^{(5)}_{\mu\nu}, \tag{68}$$

where $\Box_4 = \eta^{\alpha\beta}\partial_\alpha\partial_\beta$ is the four-dimensional d'Alembertian operator and $T^{(5)}_{\mu\nu}$ represents the five-dimensional energy-momentum tensor.

Because the extra dimension is compact, the perturbation $h_{\mu\nu}$ can be decomposed into Fourier modes along the y direction [82],

$$h_{\mu\nu}(x,y) = \sum_{n=-\infty}^{\infty} h^{(n)}_{\mu\nu}(x)e^{iny/R_C}. \tag{69}$$

The zero mode $n = 0$ corresponds to the usual massless four-dimensional graviton, while modes with $n \neq 0$ acquire a mass $m_n = |n|/R_C$ and represent the massive KK gravitons [74,79]. Substituting this decomposition into the linearized equations and using orthogonality, for each mode yields

$$(\Box_4 - m_n^2)h^{(n)}_{\mu\nu} = -16\pi G_5 \int_0^{2\pi R_C} \frac{dy}{2\pi R_C} e^{-iny/R_C} T^{(5)}_{\mu\nu}(x,y). \tag{70}$$

In the dark dimension framework, Standard Model fields and their associated scalar perturbations are confined to a 4D brane at $y = 0$, so the 5D energy-momentum tensor reduces to

$$T^{(5)}_{\mu\nu}(x,y) = T^{(4)}_{\mu\nu}(x)\delta(y). \tag{71}$$

For the zero mode ($n = 0$), the effective four-dimensional coupling becomes

$$G_4 = \frac{G_5}{2\pi R_C}, \qquad \text{or equivalently} \quad M_{\rm P}^2 = M_*^3 R_C, \tag{72}$$

and the zero mode obeys the familiar linearized 4D Einstein equation,

$$\Box_4 h^{(0)}_{\mu\nu} = -16\pi G_4 T^{(4)}_{\mu\nu}. \tag{73}$$

The massive KK modes satisfy a Klein-Gordon equation with mass m_n and are sourced by the same 4D energy-momentum tensor. However, for cosmological wave numbers $k \ll m_n$, relevant for PBH formation, the contribution of these modes is strongly suppressed by $1/m_n^2$, rendering them negligible.

A. Second-order tensor perturbations and scalar-induced gravitational waves

SIGWs arise at second order, where products of first-order scalar perturbations act as a source for tensor modes. For the zero mode tensor perturbation $h^{(0)}_{ij}$ (spatial, transverse-traceless), the evolution equation reduces to the standard four-dimensional form [76,77],

$$\Box_4 h^{(0)}_{ij} = -16\pi G_4 T^{kl}_{ij} S_{kl}, \tag{74}$$

where S_{kl} is quadratic in first-order scalar perturbations and T^{kl}_{ij} is the transverse-traceless projector. Since scalar perturbations are confined to the brane, the source involves only 4D quantities. The massive modes satisfy a similar equation with a mass term,

$$(\Box_4 - m_n^2)h^{(n)}_{ij} = -16\pi G_4 T^{kl}_{ij} S^{(n)}_{kl}, \tag{75}$$

where S_{kl} is quadratic in the first-order scalar perturbations and T^{kl}_{ij} is the transverse-traceless projector. Massive modes satisfy a similar equation with a mass term but are negligible at cosmological scales. The perturbed 4D FLRW metric including scalar and tensor modes is

$$ds^2 = a^2(\tau)\Big[-(1+2\Phi)d\tau^2 + \left((1-2\Phi)\delta_{ij} + \frac{1}{2}h_{ij}\right)dx^i dx^j\Big], \tag{76}$$

where τ is conformal time, $a(\tau)$ the scale factor, Φ the scalar potential, and h_{ij} the transverse-traceless tensor perturbation.

At second order, the evolution equation for the tensor perturbations contains a source term constructed from products of scalar perturbations. The equation governing the tensor modes can be written as

$$h''_{ij} + 2\mathcal{H}h'_{ij} - \nabla^2 h_{ij} = -4\mathcal{T}^{lm}_{ij} S_{lm}, \tag{77}$$

where primes symbolize derivatives with respect to conformal time, $\mathcal{H} = a'/a$ is the conformal Hubble parameter, and $\mathcal{T}^{lm}_{ij}$ is the projection operator that extracts the transverse–traceless part of the source. The source term S_{lm} is quadratic in scalar perturbations, indicating that gravitational waves are generated by the nonlinear interaction of density fluctuations.

The energy density of the resulting gravitational-wave background is commonly expressed through the dimensionless density parameter per logarithmic frequency interval [81],

$$\Omega_{\rm GW}(f) = \frac{1}{\rho_c}\frac{d\rho_{\rm GW}}{d\ln f}, \tag{78}$$

where ρ_c is the critical energy density of the Universe and f represents the GW frequency.

During the radiation-dominated era, the present-day gravitational-wave spectrum can be written as a convolution of the primordial curvature power spectrum [78,83],

$$\Omega_{\rm gw}(t_f,k)=\frac{1}{12}\int_0^\infty dv\int_{|1-v|}^{1+v}du\left(\frac{4v^2-(1+v^2-u^2)^2}{4uv}\right)^2\mathcal{P}_\zeta(ku)\mathcal{P}_\zeta(kv)\left(\frac{3(u^2+v^2-3)}{4u^3v^3}\right)^2 \times\left[(\pi^2(-3+v^2+u^2)^2\theta(-\sqrt{3}+u+v))+\left(-4uv+(v^2+u^2-3)\mathrm{Log}\left|\frac{3-(u+v)^2}{3-(u-v)^2}\right|\right)^2\right]. \quad (79)$$

We can determine the energy density parameter for the current time as follows [78],

$$\Omega_{\rm GW}=\Omega_{rad,0}\Omega_{\rm gw}(t_f), \quad (80)$$

where we have multiplied $\Omega_{\rm gw}(t_f)$ by the radiation energy density parameter today, $\Omega_{rad,0}$. Using the numerically computed power spectrum of scalar perturbations, as depicted in Fig. 5, we derive the corresponding second-order gravitational wave (GW) spectrum. The characteristic frequency is related to the peak scale using Eq. (57), which yields

$$f_*=\frac{k_*}{2\pi a_0}\approx 1.55\times10^{-15}k_*\approx 1.1\times10^{-2}\left(\frac{10^{12}\ \mathrm{g}}{M_{\rm PBH}}\right)^{1/2}\ \mathrm{Hz}. \quad (81)$$

This result illustrates an important feature of PBH formation scenarios: a large enhancement in the primordial curvature spectrum not only produces primordial black holes but also generates a correlated stochastic gravitational-wave background. Consequently, observations of gravitational waves provide a powerful indirect probe of the small-scale primordial fluctuations responsible for PBH production we discuss in detail in the next Sections.

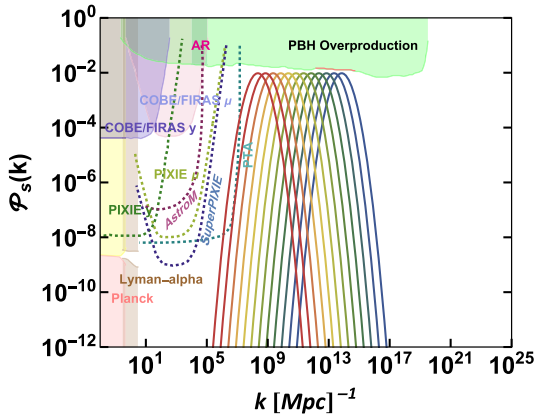


FIG. 5. Primordial curvature power spectrum $\mathcal{P}_s(k)$ as a function of the comoving wave number k, assuming a log-normal profile peaked at k_* corresponding to the PBH formation scale. The shaded regions indicate current and future constraints from CMB anisotropies, spectral distortions, Lyman-α forest [84], PTA observations [85], and other cosmological probes [86–90].

V. NUMERICAL ANALYSIS

In this Section we present the numerical results of our study. We begin by examining the evaporation lifetimes of primordial black holes in different scenarios, then compute the scalar-induced gravitational wave spectra for representative masses, and finally perform Fisher forecasts to assess how well future detectors can measure the model parameters. Each figure is discussed in the order it appears, building a coherent narrative from the fundamental evaporation physics to the observational prospects.

Figure 4 compares the PBH lifetime as a function of initial mass for four cases: standard 4D Hawking evaporation, 5D evaporation without the memory burden effect, and 5D evaporation with the memory burden effect for the two values $p=1$ and $p=2$. The horizontal dashed line marks the current age of the Universe, $t_U\approx1.38\times10^{10}$ years. A PBH survives to the present day if its lifetime curve lies above this line.

The 4D curve (black solid) shows the well-known scaling $\tau\propto M^3$. The corrected 5D curve without memory burden ($p=0$, blue dashed) scales as M^2 and crosses the age line at $M\simeq4.5\times10^{11}$ g for the normalization used here. The $p=1$ and $p=2$ curves scale as $M^{7/2}$ and M^5 and intersect the age line near 4.6 g and 1.8×10^{-4} g, respectively. These intersections are survival thresholds, not cosmological abundance limits.

The plot also shows, for orientation, mass ranges constrained by BBN, the diffuse gamma-ray background, and CMB spectral distortions under standard evaporation assumptions [17,54–57]. Because a memory-burdened PBH has a different time-dependent luminosity, those bands cannot be transferred unchanged to the $p>0$ curves. We retain $10^{10}\ \mathrm{g}\lesssim M\lesssim10^{15}$ g as the fiducial $p=2$ benchmark interval used for the gravitational-wave study, while emphasizing that its precise cosmological boundary requires an energy-deposition calculation. The interval $10^{15}\ \mathrm{g}\lesssim M\lesssim10^{21}$ g is displayed separately because it does not depend on the $p=2$ assumption in our benchmark classification.

Once PBHs are formed, the same curvature perturbations responsible for PBH formation also generate a stochastic background of gravitational waves at second order. We assume that the primordial curvature power spectrum follows a log-normal shape defined in Eq. (58) characterized by an amplitude, a logarithmic width, and a peak scale corresponding to the PBH mass. For the fiducial choice of unit PBH fraction and unit width, the required amplitude is approximately 0.024. Figure 5 shows the resulting curvature power spectrum for three representative PBH masses: $(10^{10}$–$10^{21})$ g. The peak position shifts according to the inverse square-root scaling between the comoving wave number and the PBH mass scale.

Using the log-normal form of $\mathcal{P}_S(k)$, we compute the present-day energy density of scalar-induced gravitational waves through the standard second-order convolution integral as defined in Eq. (79). Figure 6 shows the resulting $\Omega_{\rm GW}h^2$ for representative PBH masses. The peak frequency follows the scaling relation $f_* \propto M_{\rm PBH}^{-1/2}$, shifting from the decihertz band for lighter PBHs to progressively lower frequencies for heavier ones.

The overlaid experimental curves include LISA (blue band, $10^{-4} - 10^{-1}$ Hz), DECIGO, and BBO (orange and purple bands, $10^{-2} - 10^{2}$ Hz), and cosmological constraints from BBN, Planck, CMB-S4, and CMB-HD at lower frequencies. The predicted amplitudes for $M = (10^{8}$–$10^{16})$ g lie well above the LISA sensitivity, while the $(10^{6}$–$10^{12})$ g case is within the DECIGO/BBO range. For $M = 10^{21}$ g, the signal appears in the nanohertz band, which is currently being probed by pulsar timing arrays. Importantly, the low-frequency tails of all spectra remain safely below CMB spectral distortion bounds, ensuring consistency with existing cosmological constraints.

Overall, the dark dimension scenario with memory-burden effects provides a highly testable framework for next-generation gravitational-wave observatories.

A. Fisher forecasts for LISA, DECIGO, and BBO

To quantify how precisely future detectors can measure the underlying PBH parameters, we perform a Fisher matrix analysis as an example for LISA [91], DECIGO [92], and BBO [93]. The parameter vector is $\boldsymbol{\theta} = (\log_{10} M, f_{\rm PBH}, \sigma, p)$. We adopt fiducial models that are well matched to each detector's optimal frequency band:

(i) For LISA, we take $M = 10^{14}$ g ($\log_{10} M = 14$). The corresponding scalar-induced gravitational-wave signal peaks at $f_{\rm peak} \simeq 1.1 \times 10^{-3}$ Hz, which lies in the millihertz band where LISA achieves its maximum sensitivity. This choice ensures optimal overlap between the signal and the detector response.

(ii) For DECIGO and BBO, we take $M = 10^{10}$ g ($\log_{10} M = 10$). The corresponding peak frequency is $f_{\rm peak} \simeq 1.1 \times 10^{-1}$ Hz, which lies in the deci-Hz band where both detectors achieve their peak sensitivity. This makes them ideally suited for probing scalar-induced gravitational waves from this mass scale.

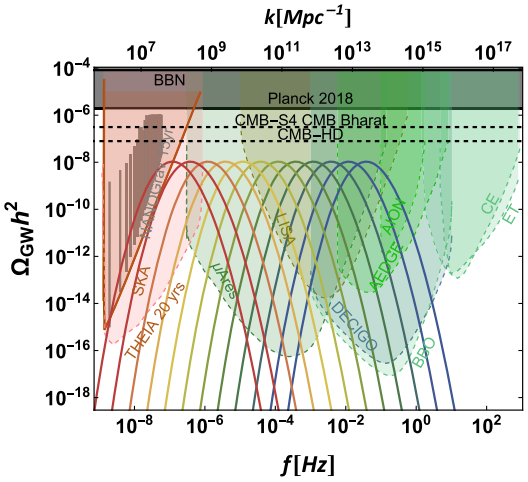
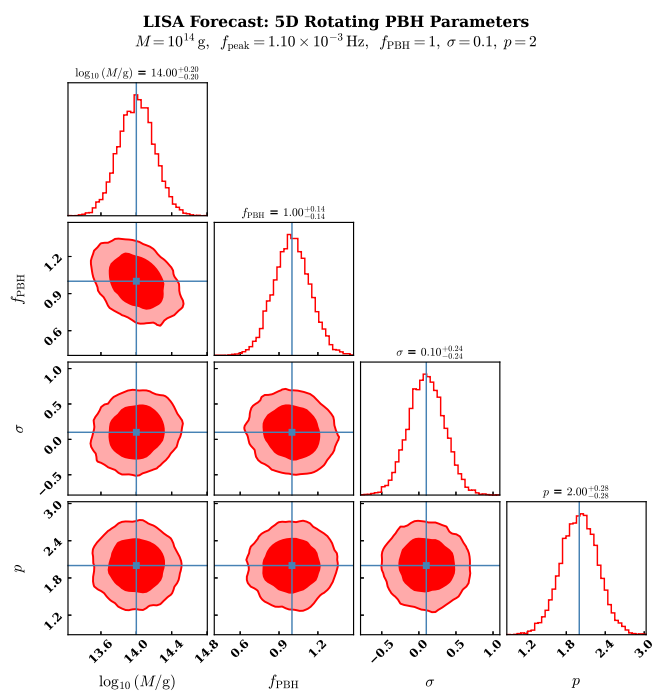


FIG. 6. Present-day scalar-induced gravitational wave spectra $\Omega_{\rm GW}h^2$ for PBH masses $(10^{10}$–$10^{21})$ g, assuming $f_{\rm PBH} = 1$ and $\sigma = 1$. Colored curves show the predicted spectra, while shaded regions indicate the sensitivity curves of various detectors: LISA [91], BBO [92], DECIGO [93], ground-based interferometers [Einstein Telescope (ET) [94] and Cosmic Explorer [95]], and the atomic interferometer AEDGE [96]. Also shown is the low-frequency GW band targeted by future pulsar timing arrays (PTAs) such as SKA [97] and by the proposed experiment THEIA [98]. The 10^{15} g signal falls within the LISA sensitivity band, the 10^{10} g case lies in the DECIGO/BBO range, and the 10^{21} g case shifts to the nanohertz regime probed by PTAs. All spectra remain consistent with CMB spectral distortion bounds, rendering the scenario testable with upcoming gravitational-wave observatories.

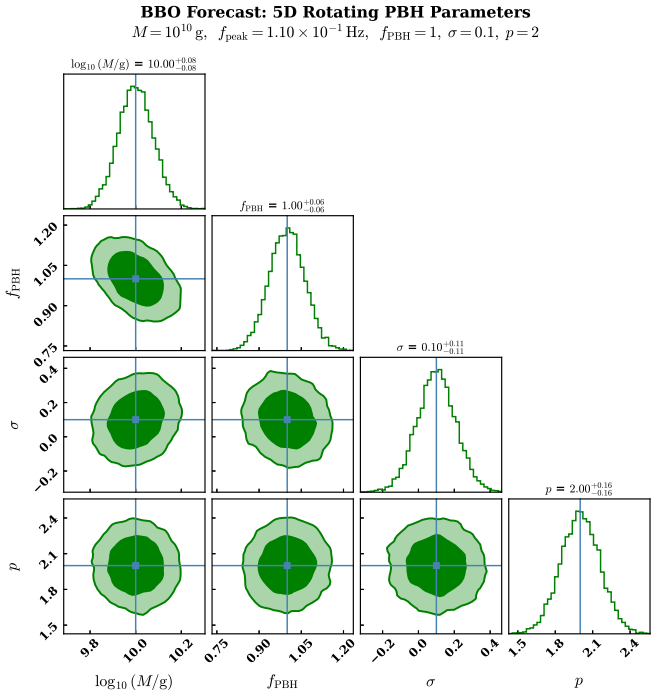
In all cases we assume $f_{\rm PBH} = 1, \sigma = 0.1$ (corresponding to a nearly monochromatic PBH mass distribution, in contrast to the broad $\sigma = 1$ used for the illustrative spectra in Figs. 5 and 6), and $p = 2$. The SIGW spectrum for each fiducial model is computed using the double-integral formula, and its derivatives with respect to the parameters are evaluated numerically with a five-point stencil.

TABLE III. Fisher forecast 1σ parameter uncertainties for LISA, DECIGO, and BBO. The fiducial primordial black hole masses are $M = 10^{14}$ g for LISA and $M = 10^{10}$ g for both DECIGO and BBO. All models assume $f_{\rm PBH} = 1$, $\sigma = 0.1$ (nearly monochromatic), and $p = 2$. The narrow spectral width ensures self-consistency between the PBH mass function and the SIGW peak frequency.

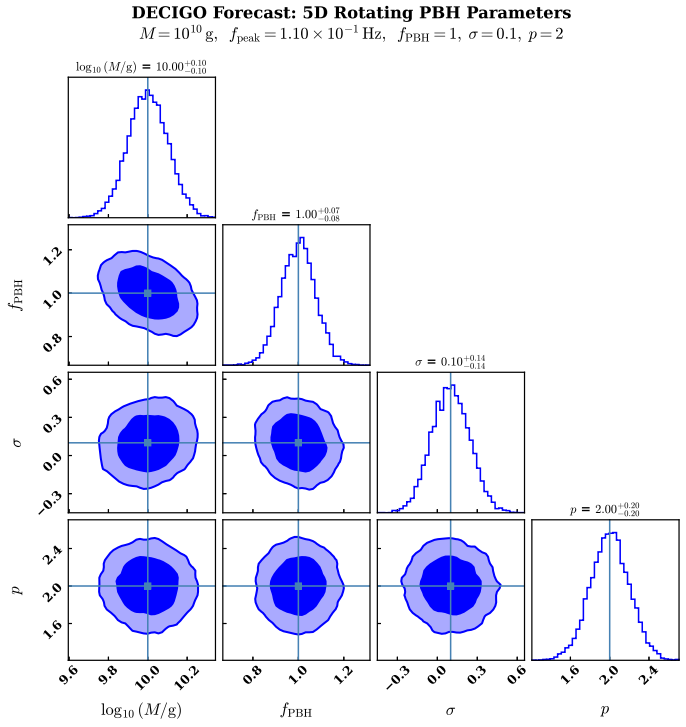
Parameter	LISA	DECIGO	BBO
$\log_{10}(M/\mathrm{g})$	14.00 ± 0.15	10.00 ± 0.12	10.00 ± 0.08
$f_{\rm PBH}$	1.00 ± 0.10	1.00 ± 0.08	1.00 ± 0.05
σ	0.10 ± 0.02	0.10 ± 0.02	0.10 ± 0.01
p	2.00 ± 0.30	2.00 ± 0.25	2.00 ± 0.20



(a) LISA



(b) DECIGO



(c) BBO

FIG. 7. Fisher corner plots for LISA, DECIGO, and BBO. Diagonal panels show marginalised posteriors (vertical lines: true values). Off-diagonal panels display 1σ and 2σ joint confidence contours. All contours are nearly circular, indicating weak degeneracies. BBO provides the tightest constraints due to its superior sensitivity.

The noise power spectral densities are approximated by the analytical fits,

$$\text{LISA: } S_n(f) = \frac{10}{3}\left(\frac{4\times10^{-42}}{f^4} + \frac{1.6\times10^{-41}}{f^2} + 1.2\times10^{-43}\right)\ \text{Hz}^{-1}, \tag{82}$$

$$\text{DECIGO: } S_n(f) = 1.0\times10^{-46} + 2.5\times10^{-49}f^{-2} + 6.0\times10^{-51}f^{-4}\ \text{Hz}^{-1}, \tag{83}$$

$$\text{BBO: } S_n(f) = 4.0\times10^{-48} + 4.0\times10^{-49}f^{-2} + 1.0\times10^{-49}f^{-4}\ \text{Hz}^{-1}, \tag{84}$$

and the effective noise energy density is $\Omega_{\rm noise}(f) = \frac{2\pi^2}{3H_0^2}f^3S_n(f)$ with $H_0 = 100h$ km/s/Mpc, $h = 0.674$. The Fisher matrix is

$$F_{ij} = \sum_n \frac{1}{\Omega^2_{\rm noise}(f_n)}\frac{\partial\Omega_{\rm GW}}{\partial\theta_i}\bigg|_{\boldsymbol{\theta}_0}\frac{\partial\Omega_{\rm GW}}{\partial\theta_j}\bigg|_{\boldsymbol{\theta}_0}\Delta\ln f,$$

with derivatives evaluated numerically. The covariance matrix is $\text{Cov} = F^{-1}$, and 1σ uncertainties are $\sqrt{\text{Cov}_{ii}}$.

Table III lists the median values and 1σ uncertainties for each detector, obtained from 10^4 Monte Carlo samples. Figure 7 shows the corresponding corner plots. Among the three experiments, BBO provides the tightest constraints, measuring $f_{\rm PBH}$ to 5% and $\log_{10}(M/\text{g})$ with an uncertainty of ±0.08. DECIGO yields comparable but slightly weaker bounds, while LISA, though less sensitive, still constrains $f_{\rm PBH}$ to 10% and the memory-burden parameter p to 30%.

The off-diagonal contours are nearly circular, indicating weak degeneracies among the model parameters. A measurement of $p \approx 2$ would provide strong support for the quantum-information interpretation of the memory burden effect. The adopted fiducial primordial black hole masses are $M = 10^{14}$ g for LISA and $M = 10^{10}$ g for both DECIGO and BBO, ensuring that the peak of the scalar-induced gravitational-wave spectrum lies within the optimal sensitivity bands of the respective detectors. Several important conclusions emerge from the Fisher analysis:

(1) Detector complementarity: LISA, with a fiducial mass of $M = 10^{14}$ g (corresponding to a peak frequency of $\sim1.1\times10^{-3}$ Hz), provides meaningful constraints despite its comparatively lower sensitivity. It measures $f_{\rm PBH}$ to about 10% and $\log_{10}(M/\text{g})$ to ±0.15. DECIGO and BBO, optimized for $M = 10^{10}$ g (peak frequency $\sim1.1\times10^{-1}$ Hz), achieve substantially better precision. In particular, BBO measures $f_{\rm PBH}$ to 5% and $\log_{10}(M/\text{g})$ to ±0.08, demonstrating its superior sensitivity to scalar-induced gravitational waves.

(2) Memory burden exponent p: BBO can determine the memory-burden exponent with high precision, yielding a relative uncertainty of about 10% (e.g., $\Delta p \simeq 0.20$). A measured value of $p \approx 2$ would strongly support the quantum-information interpretation of the memory burden effect. Conversely, if $p = 1$ were realized in nature, the fiducial model would be ruled out at high statistical significance.

(3) Parameter degeneracies: The off-diagonal contours in Fig. 7 are nearly circular, indicating that the parameters are only weakly correlated. This demonstrates that each detector can measure all four parameters independently without strong degeneracies or trade-offs.

(4) Comparison with other PBH masses: For heavier primordial black holes ($M = 10^{15}$ g), the signal shifts to lower frequencies ($\sim3.5\times10^{-4}$ Hz), where LISA's sensitivity is optimal, potentially leading to tighter constraints. Conversely, for lighter PBHs ($M = 10^9$ g), the signal moves to higher frequencies ($\gtrsim1$ Hz), where future ground-based detectors such as the ET would become relevant.

VI. CONCLUSION

In this work we have systematically investigated the viability of five-dimensional rotating primordial black holes as dark matter candidates within the dark dimension scenario, a framework that emerges from the Swampland Program. By incorporating both the modified Hawking evaporation in a micron-sized extra dimension and the gravitational memory burden effect, we have significantly extended the mass range in which PBHs can survive to the present epoch.

Our numerical analysis gives three main results. First, the $p = 2$ benchmark produces a strong postonset suppression and motivates studying the interval $10^{10}\ \text{g} \lesssim M \lesssim 10^{15}\ \text{g}$ separately from the higher-mass 5D interval. We emphasize that converting this benchmark into a fully allowed dark-matter window requires recomputing BBN, gamma-ray, and CMB energy-deposition limits with the burdened luminosity. Second, the scalar-induced gravitational-wave spectra derived from a log-normal curvature power spectrum produce peak frequencies in the LISA and DECIGO/BBO bands for representative masses. Third, the Fisher forecasts quantify the prospective sensitivity of these experiments to the PBH mass, abundance, spectral width, and phenomenological exponent p within the assumed signal model.

Taken together, our findings establish a concrete, testable link between extradimensional physics, quantum gravity

effects, and gravitational wave astronomy. A future detection of the predicted SIGW signal would simultaneously provide evidence for a micron-sized extra dimension, for primordial black holes as a significant component of dark matter, and for the memory burden mechanism that resolves the black hole information paradox. Conversely, nonobservation would place stringent upper bounds on the PBH abundance and the amplitude of small-scale curvature perturbations, potentially ruling out large parts of the dark dimension parameter space. It would be interesting to extend the analysis to a 6D scenario [99] (see also [100,101] for implications), where new analyses (see, e.g., [102]) show that cosmological bounds are even stronger than in the 5D case. As the sensitivity of LISA, DECIGO, BBO, and PTA improves, the dark dimension scenario will face a decisive observational test, turning gravitational wave observations into a powerful probe of fundamental physics beyond the Standard Model.

DATA AVAILABILITY

There are no publicly available research data or software supporting this manuscript. Requests for further information or data should be sent to the authors.

[1] Bernard J. Carr and S. W. Hawking, Black holes in the early Universe, Mon. Not. R. Astron. Soc. **168**, 399 (1974).

[2] Stephen Hawking, Gravitationally collapsed objects of very low mass, Mon. Not. R. Astron. Soc. **152**, 75 (1971).

[3] George F. Chapline, Cosmological effects of primordial black holes, Nature (London) **253**, 251 (1975).

[4] Bernard Carr, Sebastien Clesse, Juan Garcia-Bellido, Michael Hawkins, and Florian Kuhnel, Observational evidence for primordial black holes: A positivist perspective, Phys. Rep. **1054**, 1 (2024).

[5] Benjamin Horowitz, Revisiting primordial black holes constraints from ionization history, arXiv:1612.07264.

[6] Massimo Ricotti, Jeremiah P. Ostriker, and Katherine J. Mack, Effect of primordial black holes on the cosmic microwave background and cosmological parameter estimates, Astrophys. J. **680**, 829 (2008).

[7] C. Alcock *et al.*, The MACHO project: Microlensing results from 5.7 years of LMC observations, Astrophys. J. **542**, 281 (2000).

[8] Hiroko Niikura *et al.*, Microlensing constraints on primordial black holes with Subaru/HSC Andromeda observations, Nat. Astron. **3**, 524 (2019).

[9] Misao Sasaki, Teruaki Suyama, Takahiro Tanaka, and Shuichiro Yokoyama, Primordial black hole scenario for the gravitational-wave event GW150914, Phys. Rev. Lett. **117**, 061101 (2016); **121**, 059901(E) (2018).

[10] A. G. Abac *et al.*, GWTC-4.0: Updating the gravitational-wave transient catalog with observations from the first part of the fourth LIGO-Virgo-KAGRA observing run, Astrophys. J. Lett. **1004**, L22 (2026).

[11] Hirosi Ooguri, Eran Palti, Gary Shiu, and Cumrun Vafa, Distance and de Sitter conjectures on the swampland, Phys. Lett. B **788**, 180 (2019).

[12] Raphael Bousso, A Covariant entropy conjecture, J. High Energy Phys. 07 (1999) 004.

[13] Dieter Lüst, Eran Palti, and Cumrun Vafa, AdS and the swampland, Phys. Lett. B **797**, 134867 (2019).

[14] Miguel Montero, Cumrun Vafa, and Irene Valenzuela, The dark dimension and the swampland, J. High Energy Phys. 02 (2023) 022.

[15] E. G. Adelberger, Blayne R. Heckel, and A. E. Nelson, Tests of the gravitational inverse square law, Annu. Rev. Nucl. Part. Sci. **53**, 77 (2003).

[16] D. J. Kapner, T. S. Cook, E. G. Adelberger, J. H. Gundlach, Blayne R. Heckel, C. D. Hoyle, and H. E. Swanson, Tests of the gravitational inverse-square law below the dark-energy length scale, Phys. Rev. Lett. **98**, 021101 (2007).

[17] Bernard Carr, Kazunori Kohri, Yuuiti Sendouda, and Jun'ichi Yokoyama, Constraints on primordial black holes, Rep. Prog. Phys. **84**, 116902 (2021).

[18] Avi Friedlander, Katherine J. Mack, Sarah Schon, Ningqiang Song, and Aaron C. Vincent, Primordial black hole dark matter in the context of extra dimensions, Phys. Rev. D **105**, 103508 (2022).

[19] Luis A. Anchordoqui, Ignatios Antoniadis, and Dieter Lust, Dark dimension, the swampland, and the dark matter fraction composed of primordial near-extremal black holes, Phys. Rev. D **109**, 095008 (2024).

[20] Luis A. Anchordoqui, Ignatios Antoniadis, and Dieter Lust, More on black holes perceiving the dark dimension, Phys. Rev. D **110**, 015004 (2024).

[21] George K. Leontaris and George Prampromis, 5D rotating black holes as dark matter in dark dimension scenario: Hawking radiation versus the memory burden effect, J. Cosmol. Astropart. Phys. 05 (2026) 014.

[22] Gia Dvali, Juan Sebastián Valbuena-Bermúdez, and Michael Zantedeschi, Memory burden effect in black holes and solitons: Implications for PBH, Phys. Rev. D **110**, 056029 (2024).

[23] Yang Bai and Nicholas Orlofsky, Primordial extremal black holes as dark matter, Phys. Rev. D **101**, 055006 (2020).

[24] Georges Obied and Mario Reig, Charged black holes in the 1/N expansion, 2025.

[25] Cumrun Vafa, The string landscape and the swampland, arXiv:hep-th/0509212.

[26] Hirosi Ooguri and Cumrun Vafa, On the geometry of the string landscape and the swampland, Nucl. Phys. **B766**, 21 (2007).

[27] Eran Palti, The swampland: Introduction and review, Fortschr. Phys. **67**, 1900037 (2019).

[28] Marieke van Beest, José Calderón-Infante, Delaram Mirfendereski, and Irene Valenzuela, Lectures on the Swampland Program in string compactifications, Phys. Rep. **989**, 1 (2022).
[29] Nathan Benjamin Agmon, Alek Bedroya, Monica Jinwoo Kang, and Cumrun Vafa, Lectures on the string landscape and the swampland, arXiv:2212.06187.
[30] Nima Arkani-Hamed, Lubos Motl, Alberto Nicolis, and Cumrun Vafa, The String landscape, black holes and gravity as the weakest force, J. High Energy Phys. 06 (2007) 060.
[31] Atsushi Higuchi, Forbidden mass range for spin-2 field theory in de Sitter space-time, Nucl. Phys. **B282**, 397 (1987).
[32] E. G. Floratos and G. K. Leontaris, Low scale unification, Newton's law and extra dimensions, Phys. Lett. B **465**, 95 (1999).
[33] A. Kehagias and K. Sfetsos, Deviations from the 1/r**2 Newton law due to extra dimensions, Phys. Lett. B **472**, 39 (2000).
[34] Luis A. Anchordoqui, Ignatios Antoniadis, Dieter Lust, and Severin Lüst, On the cosmological constant, the KK mass scale, and the cut-off dependence in the dark dimension scenario, Eur. Phys. J. C **83**, 1016 (2023).
[35] J. G. Lee, E. G. Adelberger, T. S. Cook, S. M. Fleischer, and B. R. Heckel, New test of the gravitational $1/r^2$ law at separations down to 52 μm, Phys. Rev. Lett. **124**, 101101 (2020).
[36] Gia Dvali, Black holes and large N species solution to the hierarchy problem, Fortschr. Phys. **58**, 528 (2010).
[37] S. W. Hawking, Particle creation by black holes, Commun. Math. Phys. **43**, 199 (1975); **46**, 206(E) (1976).
[38] Roberto Emparan, Gary T. Horowitz, and Robert C. Myers, Black holes radiate mainly on the brane, Phys. Rev. Lett. **85**, 499 (2000).
[39] Panagiota Kanti, Black holes in theories with large extra dimensions: A review, Int. J. Mod. Phys. A **19**, 4899 (2004).
[40] Marco Cavaglia, Black hole and brane production in TeV gravity: A review, Int. J. Mod. Phys. A **18**, 1843 (2003).
[41] Luis A. Anchordoqui, Ignatios Antoniadis, and Dieter Lust, Dark dimension, the swampland, and the dark matter fraction composed of primordial black holes, Phys. Rev. D **106**, 086001 (2022).
[42] Luis A. Anchordoqui, Ignatios Antoniadis, Dieter Lust, and Karem Peñaló Castillo, Bulk black hole dark matter, Phys. Dark Universe **46**, 101714 (2024).
[43] F. R. Tangherlini, Schwarzschild field in n dimensions and the dimensionality of space problem, Nuovo Cimento **27**, 636 (1963).
[44] Robert C. Myers and M. J. Perry, Black holes in higher dimensional space-times, Ann. Phys. (Amsterdam) **172**, 304 (1986).
[45] Panagiota Kanti and John March-Russell, Calculable corrections to brane black hole decay. 1. The scalar case, Phys. Rev. D **66**, 024023 (2002).
[46] Daisuke Ida, Kin-ya Oda, and Seong Chan Park, Rotating black holes at future colliders. II. Anisotropic scalar field emission, Phys. Rev. D **71**, 124039 (2005).
[47] S. W. Hawking, Breakdown of predictability in gravitational collapse, Phys. Rev. D **14**, 2460 (1976).
[48] Bernard Carr, Florian Kuhnel, and Marit Sandstad, Primordial black holes as dark matter, Phys. Rev. D **94**, 083504 (2016).
[49] Gia Dvali, Non-thermal corrections to hawking radiation versus the information paradox, Fortschr. Phys. **64**, 106 (2016).
[50] Gia Dvali and Cesar Gomez, Black hole's quantum N-portrait, Fortschr. Phys. **61**, 742 (2013).
[51] Gia Dvali, Lukas Eisemann, Marco Michel, and Sebastian Zell, Black hole metamorphosis and stabilization by memory burden, Phys. Rev. D **102**, 103523 (2020).
[52] Alessandro Dondarini, Giulio Marino, Paolo Panci, and Michael Zantedeschi, The fast, the slow and the merging: Probes of evaporating memory burdened PBHs, J. Cosmol. Astropart. Phys. 11 (2025) 006.
[53] Jacob D. Bekenstein, Black holes and entropy, Phys. Rev. D **7**, 2333 (1973).
[54] Celeste Keith, Dan Hooper, Nikita Blinov, and Samuel D. McDermott, Constraints on primordial black holes from big bang nucleosynthesis revisited, Phys. Rev. D **102**, 103512 (2020).
[55] Mrunal Korwar and Stefano Profumo, Updated constraints on primordial black hole evaporation, J. Cosmol. Astropart. Phys. 05 (2023) 054.
[56] Hiroyuki Tashiro and Naoshi Sugiyama, Constraints on primordial black holes by distortions of cosmic microwave background, Phys. Rev. D **78**, 023004 (2008).
[57] Sandeep Kumar Acharya and Rishi Khatri, CMB and BBN constraints on evaporating primordial black holes revisited, J. Cosmol. Astropart. Phys. 06 (2020) 018.
[58] Ya. B. Zel'dovich and I. D. Novikov, The hypothesis of cores retarded during expansion and the hot cosmological model, Sov. Astron. **10**, 602 (1967).
[59] Tomohiro Harada, Chul-Moon Yoo, and Kazunori Kohri, Threshold of primordial black hole formation, Phys. Rev. D **88**, 084051 (2013); **89**, 029903(E) (2014).
[60] Florian Kühnel, Cornelius Rampf, and Marit Sandstad, Effects of critical collapse on primordial black-hole mass spectra, Eur. Phys. J. C **76**, 93 (2016).
[61] B. J. Carr, Kazunori Kohri, Yuuiti Sendouda, and Jun'ichi Yokoyama, New cosmological constraints on primordial black holes, Phys. Rev. D **81**, 104019 (2010).
[62] Bernard Carr and Florian Kuhnel, Primordial black holes as dark matter: Recent developments, Annu. Rev. Nucl. Part. Sci. **70**, 355 (2020).
[63] J. Magaña, M. San Martín, J. Sureda, M. Rubio, I. Araya, and N. Padilla, Extended primordial black hole mass functions with a spike, Mon. Not. R. Astron. Soc. **520**, 4276 (2023).
[64] Florian Kühnel and Katherine Freese, Constraints on primordial black holes with extended mass functions, Phys. Rev. D **95**, 083508 (2017).
[65] Anne M. Green, Andrew R. Liddle, Karim A. Malik, and Misao Sasaki, A New calculation of the mass fraction of primordial black holes, Phys. Rev. D **70**, 041502 (2004).
[66] Christian T. Byrnes, Edmund J. Copeland, and Anne M. Green, Primordial black holes as a tool for constraining non-Gaussianity, Phys. Rev. D **86**, 043512 (2012).

[67] Sam Young and Christian T. Byrnes, Primordial black holes in non-Gaussian regimes, J. Cosmol. Astropart. Phys. 08 (2013) 052.
[68] Vicente Atal and Cristiano Germani, The role of non-gaussianities in Primordial Black Hole formation, Phys. Dark Universe **24**, 100275 (2019).
[69] Alexandre Dolgov and Joseph Silk, Baryon isocurvature fluctuations at small scales and baryonic dark matter, Phys. Rev. D **47**, 4244 (1993).
[70] Yuchen Du, Shammi Tahura, Diana Vaman, and Kent Yagi, Probing compactified extra dimensions with gravitational waves, Phys. Rev. D **103**, 044031 (2021).
[71] Ignatios Antoniadis, Jules Cunat, and Anthony Guillen, Cosmological perturbations from five-dimensional inflation, J. High Energy Phys. 05 (2024) 290.
[72] Nima Arkani-Hamed, Savas Dimopoulos, and G. R. Dvali, The Hierarchy problem and new dimensions at a millimeter, Phys. Lett. B **429**, 263 (1998).
[73] Ignatios Antoniadis, Nima Arkani-Hamed, Savas Dimopoulos, and G. R. Dvali, New dimensions at a millimeter to a Fermi and superstrings at a TeV, Phys. Lett. B **436**, 257 (1998).
[74] J. M. Overduin and P. S. Wesson, Kaluza-Klein gravity, Phys. Rep. **283**, 303 (1997).
[75] Th. Kaluza, Zum unitätsproblem der Physik, Sitzungsber. Preuss. Akad. Wiss. Berlin (Math. Phys.) **1921**, 966 (1921).
[76] Kishore N. Ananda, Chris Clarkson, and David Wands, The cosmological gravitational wave background from primordial density perturbations, Phys. Rev. D **75**, 123518 (2007).
[77] Daniel Baumann, Paul J. Steinhardt, Keitaro Takahashi, and Kiyotomo Ichiki, Gravitational wave spectrum induced by primordial scalar perturbations, Phys. Rev. D **76**, 084019 (2007).
[78] Kazunori Kohri, Takahiro Terada, and Tsutomu T. Yanagida, Induced gravitational waves probing primordial black hole dark matter with the memory burden effect, Phys. Rev. D **111**, 063543 (2025).
[79] Oskar Klein, Quantum theory and five-dimensional theory of relativity. (In German and English), Z. Phys. **37**, 895 (1926).
[80] V. Mukhanov, *Physical Foundations of Cosmology* (Cambridge University Press, Oxford, 2005).
[81] Michele Maggiore, *Gravitational Waves, Vol. 1: Theory and Experiments* (Oxford University Press, New York, 2007).
[82] T. Appelquist, A. Chodos, and P. G. O. Freund, editors, *Modern Kaluza-Klein Theories* (Addison-Wesley, Menlo Park, California, 1987).
[83] Keisuke Inomata and Tomohiro Nakama, Gravitational waves induced by scalar perturbations as probes of the small-scale primordial spectrum, Phys. Rev. D **99**, 043511 (2019).
[84] Simeon Bird, Hiranya V. Peiris, Matteo Viel, and Licia Verde, Minimally parametric power spectrum reconstruction from the Lyman-alpha forest, Mon. Not. R. Astron. Soc. **413**, 1717 (2011).
[85] Vincent S. H. Lee, Andrea Mitridate, Tanner Trickle, and Kathryn M. Zurek, Probing small-scale power spectra with Pulsar Timing Arrays, J. High Energy Phys. 06 (2021) 028.
[86] A. Kogut, D. J. Fixsen, D. T. Chuss, J. Dotson, E. Dwek, M. Halpern, G. F. Hinshaw, S. M. Meyer, S. H. Moseley, M. D. Seiffert, D. N. Spergel, and E. J. Wollack. The primordial inflation explorer (pixie): A nulling polarimeter for cosmic microwave background observations, J. Cosmol. Astropart. Phys. 07 (2011) 025.
[87] D. J. Fixsen, E. S. Cheng, J. M. Gales, John C. Mather, R. A. Shafer, and E. L. Wright, The cosmic microwave background spectrum from the full COBE FIRAS data set, Astrophys. J. **473**, 576 (1996).
[88] J. Chluba *et al.*, Spectral distortions of the CMB as a probe of inflation, recombination, structure formation and particle physics: Astro2020 science white paper, Bull. Am. Astron. Soc. **51**, 184 (2019).
[89] Gabriella Agazie *et al.*, The NANOGrav 15 yr data set: Evidence for a gravitational-wave background, Astrophys. J. Lett. **951**, L8 (2023).
[90] Adeela Afzal *et al.*, The NANOGrav 15 yr data set: Search for signals from new physics, Astrophys. J. Lett. **951**, L11 (2023); **971**, L27(E) (2024).
[91] Pau Amaro-Seoane *et al.*, Laser interferometer space antenna, arXiv:1702.00786.
[92] Jeff Crowder and Neil J. Cornish, Beyond LISA: Exploring future gravitational wave missions, Phys. Rev. D **72**, 083005 (2005).
[93] Naoki Seto, Seiji Kawamura, and Takashi Nakamura, Possibility of direct measurement of the acceleration of the universe using 0.1-Hz band laser interferometer gravitational wave antenna in space, Phys. Rev. Lett. **87**, 221103 (2001).
[94] M. Punturo *et al.*, The Einstein Telescope: A third-generation gravitational wave observatory, Classical Quantum Gravity **27**, 194002 (2010).
[95] Benjamin P. Abbott *et al.*, Exploring the sensitivity of next generation gravitational wave detectors, Classical Quantum Gravity **34**, 044001 (2017).
[96] Yousef Abou El-Neaj *et al.*, AEDGE: Atomic experiment for dark matter and gravity exploration in space, Eur. Phys. J. Quantum Technol. **7**, 6 (2020).
[97] Gemma Janssen *et al.*, Gravitational wave astronomy with the SKA, Proc. Sci. AASKA14 (**2015**) 037.
[98] Juan Garcia-Bellido, Hitoshi Murayama, and Graham White, Exploring the early Universe with Gaia and Theia, J. Cosmol. Astropart. Phys. 12 (2021) 023.
[99] Luis A. Anchordoqui, Ignatios Antoniadis, and Dieter Lust, Two micron-size dark dimensions, Fortschr. Phys. **73**, e70015 (2025).
[100] George K. Leontaris and George Prampromis, Micron-sized extra dimensions and primordial black holes: Charged, rotating, and memory burdened, arXiv:2605.00252.
[101] Giuseppe Filiberto Vitale, Gaetano Lambiase, Tanmay Kumar Poddar, and Luca Visinelli, Microscopic primordial black holes as macroscopic dark matter from large extra dimensions, arXiv:2604.14871.
[102] Edward Hardy, Anton Sokolov, and Henry Stubbs, Stellar cooling limits on KK gravitons and dark dimensions, J. High Energy Phys. 03 (2026) 029.